Original Article

Anisotropic Total Variation Denoising Technique for Low-Dose Cone-Beam Computed Tomography Imaging

Ho Lee*, Jeongmin Yoon[†], Eungman Lee[†]

*Department of Radiation Oncology, Yonsei University College of Medicine, [†]Department of Radiation Oncology, Seoul National University Hospital, [†]Department of Radiation Oncology, Ewha Womans University Medical Center, Seoul, Korea

This study aims to develop an improved Feldkamp-Davis-Kress (FDK) reconstruction algorithm using anisotropic total variation (ATV) minimization to enhance the image quality of low-dose cone-beam computed tomography (CBCT). The algorithm first applies a filter that integrates the Shepp-Logan filter into a cosine window function on all projections for impulse noise removal. A total variation objective function with anisotropic penalty is then minimized to enhance the difference between the real structure and noise using the steepest gradient descent optimization with adaptive step sizes. The preserving parameter to adjust the separation between the noise-free and noisy areas is determined by calculating the cumulative distribution function of the gradient magnitude of the filtered image obtained by the application of the filtering operation on each projection. With these minimized ATV projections, voxel-driven backprojection is finally performed to generate the reconstructed images. The performance of the proposed algorithm was evaluated with the catphan503 phantom dataset acquired with the use of a low-dose protocol. Qualitative and quantitative analyses showed that the proposed ATV minimization provides enhanced CBCT reconstruction images compared with those generated by the conventional FDK algorithm, with a higher contrast-to-noise ratio (CNR), lower root-mean-square-error, and higher correlation. The proposed algorithm not only leads to a potential imaging dose reduction in repeated CBCT scans via lower mA levels, but also elicits high CNR values by removing noisy corrupted areas and by avoiding the heavy penalization of striking features.

Keywords: Low-dose CBCT, FDK, Anisotropic total variation, Low mAs

Introduction

Volumetric imaging, such as cone-beam computed tomography (CBCT) or megavoltage computed tomography, is being extensively adapted as a commonly used approach in image guided radiation therapy (IGRT).[1] In particular, CBCT mounted on the gantry of the linear accelerator has been utilized not only for the patient setup, but also for the continuous monitoring of any target motion throughout the treatment delivery process.[2,3] In current protocols, the cumulative imaging dose from CBCT cannot be ignored when a patient is imaged daily during the entire treatment course that lasts 4 to 6 weeks.[4] If a reasonable image quality can be obtained with a low dose, it is obvious that compliance is ensured regarding the low dose protocol acquisition. The most practical way to reduce the dose of a CBCT system is to use either a lower tube current or a shorter exposure time per projection.[5] These attempts lead to sig-

nificantly degraded CBCT image qualities when analytical reconstruction algorithms are used, such as the Feldkamp–Davis–Kress (FDK) method,[6] because their performances are considerably influenced by the filtering process. An efficient denoising technique[7,8] is thus required to enhance the difference of the signals between the real structures and unwanted noise to achieve better CBCT image quality.

We propose an improved FDK-based CBCT reconstruction algorithm according to anisotropic filtration of projection data at low mA values. The proposed approach is based on the framework of the standard FDK algorithm. The algorithm first applies a modified filter on all projections for impulse noise removal. Anisotropic total variation (ATV) denoising is then applied on the filtered projection data. Minimizing the ATV objective function using the steepest gradient descent optimization with the use of an adaptive step size ensures that edges which have a high contrast relative to the surroundings will be preserved, and noisy pixels which have a low contrast will be smoothed. With the use of these projections with ATV denoising, the voxel-driven backprojector is finally performed to generate the reconstructed images. The effectiveness of the proposed method is demonstrated by a phantom study.

Materials and Methods

1. Filtration step for filtered projection data

A circular preweighting factor is first applied on each log-transformed projection data to avoid decreases in intensity owing to the cone angle effect. The circular preweighting of a projection is formulated as

$$P(\theta,u,v) = \frac{D}{\sqrt{D^2+u^2+v^2}} p(\theta,u,v), \qquad (1)$$

where $p(\theta, u, v)$ is the log-transformed value at position of (u, v) in a given projection at an angle θ, and D is the distance from the beam source to the detector. Each horizontal line of preweighted projection data (P) is converted to the frequency domain with the use of the 1-dimensional (1–D) Fourier transformation. The Fourier-transformed values are multiplied by the modified filter which is used as a 1–D ramp filter to suppress the highest spatial frequencies. The

modified filter consists of the product of the Shepp–Logan filter and a cosine window function defined in the frequency domain, as shown in Fig. 1. This is also expressed according to Eq. (2):

$$H(\omega) = \left|\sin\frac{\omega}{2}\right| (0.515+0.485\cos\omega), \quad -\pi<\omega<\pi. \qquad (2)$$

Each horizontal line in the preweighted projection data is converted to the frequency domain by 1–D Fourier transformation. Accordingly, the Fourier transformed horizontal line is multiplied by the modified filter. Based on the application of the inverse Fourier transformation, we can obtain filtered projection data with reduced impulse noise.

2. Anisotropic total variation minimization

A total variation (TV) denoising[9] is applied on filtered projections to enhance the difference of the signals between the striking features and unwanted noise by combining the conduction coefficient used in the anisotropic diffusion filter.[10] Minimizing the ATV objective function indicates that edges with high contrast relative to the surroundings are preserved, and noisy voxels with low contrast are smoothed. The anisotropic penalty[11] with different weights for neighbors at the same distance in the TV object function can be expressed as follows:

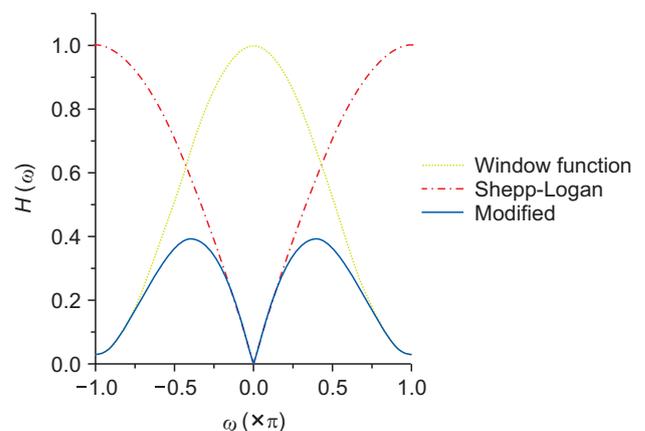$$R(P) = \sum_j R(P_j) = \sum_j w_j\, G(P_j), \qquad (3)$$

Fig. 1. 1–D ramp filter.

$$w_j = \sum_{m \in N_j} \exp\left[-\left(\frac{P_j - P_m}{\delta}\right)^2\right], \qquad (4)$$

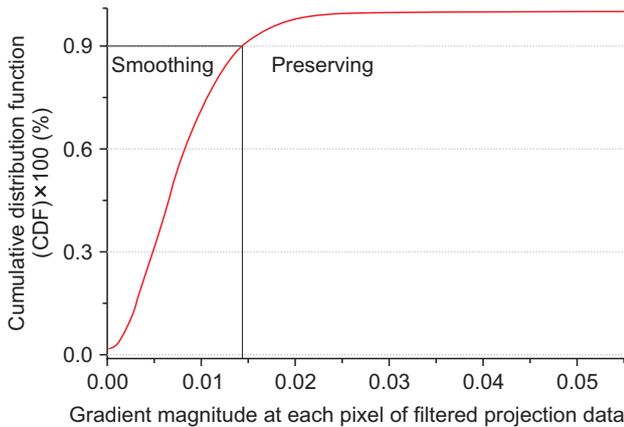$$G(P_j) = G(P_{(u,v)}) = \sqrt{(P_{(u,v)} - P_{(u-1,v)})^2 + (P_{(u,v)} - P_{(u,v-1)})^2}, \quad (5)$$

where index j identifies the index of pixel element in the filtered projection, and $P_{(u,v)}$ is the pixel element at the 2D position (u, v). Equivalently, N_j represents the set of neighbors of the jth pixel element. We only considered four first-order neighbors in the study. As shown in Fig. 2, the parameter δ was set to 90% of the cumulative distribution function (CDF) histogram. The histogram was created by accumulating the gradient magnitude at each pixel of the filtered projection data.

The ATV objective function of Eq. (3) is minimized using the steepest gradient descent method with an adaptive step size,[9,12] and is expressed as follows,

$$P_j^{t+1} = P_j^t - \lambda \frac{\nabla R(P_j)}{|\nabla R(P)|}, \qquad (6)$$

$$\lambda = \gamma \times \sqrt{\sum_j P_j^t \times P_j^t}, \qquad (7)$$

where λ is an adaptive parameter that controls the step size so that the smoothing degree is decreased in advance according to the number of iteration steps. By using the squared-root value of all pixel elements updated in each

Fig. 2. Example of the CDF plot generated with the gradient magnitude calculated at all the pixels of the filtered projection data.

steepest gradient descent step, this parameter is forced to progressively acquire smaller values as a function of the number of iterations. To avoid a local minimum owing to abrupt changes, we use a scaling parameter γ and set it to 0.1 initially. If the $R(P)$ calculated at the current iteration step is larger the value calculated at the previous step, this value is linearly decreased by multiplying a constant value. $\nabla R(P_j)$ is the gradient of the objective function $R(P)$ at the jth indexed pixel. Accordingly, the root-square sum of the gradient calculated at all pixels, $|\nabla R(P)|$, is needed for the normalized gradient calculation. The optimal number of iterations for the steepest gradient descent step was fine-tuned so that the number of noisy pixels was minimized, while the bony structures were maintained. In this study, the number of iterations for the steepest gradient descent step was set to 20.

3. Voxel−driven backprojector

Voxel-driven backprojection was performed with the ATV filtered-projection data. Given a position vector r (or the equivalent spatial coordinates r_x, r_y, and r_z) of any voxel, the corresponding ith projection data at a given angle θ and at positions u(r) and v(r) are obtained as follows,

$$P(\theta, r) = P^i(\theta, u(r), v(r)), \qquad (8)$$

where

$$u(r) = \frac{r_{x\theta}}{d + r_{y\theta}}D, \qquad (9)$$

$$v(r) = \frac{r_{z\theta}}{d + r_{y\theta}}D. \qquad (10)$$

Herein, d is the source-to-axis distance, and D is the source-to-detector distance. Accordingly, the rotation vectors $[r_{x\theta}, r_{y\theta}, r_{z\theta}]^T$ are calculated by applying the rotation matrix by a given angle θ from the origin of the reconstructed images.

The final attenuation coefficient value $\mu(r)$ at a position vector r is weighted and expressed as,

$$\mu(r) = \mu(r_x, r_y, r_z) = \frac{\pi}{N_p} \sum_{i=1}^{N_p} \left(w(r) \cdot P^i(\theta, u(r), v(r))\right), \quad (11)$$

$$w(r) = \frac{d^2}{(d+r_{y\theta})^2}, \qquad (12)$$

where $w(r)$ is the depth weighting, and N_p is the total number of projection data. Every voxel is derived from all the filtered projection data and is normalized by N_p in the backprojection step.

4. Experimental studies

Qualitative and quantitative comparisons were performed using the catphan503 (The Phantom Laboratory, Salem, NY). The phantom was aligned using the three orthogonal laser beams with its superior/inferior direction along the longitudinal direction of the couch. The CBCT projection data were acquired with XVI R5.0 (Elekta Limited, Stockholm, Sweden), which consisted of a kV radiation source mounted on the Infinity™ linear accelerator system. When the gantry rotates around the patient's couch, a series of projections was acquired with the total rotation of 360° with a small field-of-view (FOV) protocol, a S20 collimator, an F0 filter, and without a bow-tie filter. The number of projections for a full scan is approximately 665. The dimension of each projection acquried on the image receptor was 409.6×409.6 mm^2 which contained 1024×1024 pixels^2. The source-to-detector distance was 1536 mm and the source-to-axis distance was 1000 mm. For a low-dose CBCT protocol, the X-ray tube current was set to 10 mA and the duration of the X-ray pulse was 10 ms during the data acquisition of each projection. The tube voltage was set to 100 kVp. The reconstructed images were generated with a size of $512 \times 512 \times 200$ voxels^3 where the voxel size was $0.5 \times 0.5 \times 0.5$ mm^3. A high-dose CBCT for a benchmark image was created with the application of the conventional FDK algorithm with projections acquired with increased mA settings (100 kVp, 40 mA, and 40 ms) for comparison purposes. All of the reconstructed images were converted to Hounsfield units (HU).

To quantitatively compare the relative image contrast between corresponding regions, we calculated the contrast-to-noise ratio (CNR) at selected regions-of-interest (ROIs) in the reconstructed image as according to,

$$CNR = \frac{2|M_{insert} - M_{center}|}{\sqrt{\delta_{insert}^2 + \delta_{center}^2}}, \qquad (13)$$

where M_{insert} and δ_{insert} respectively denote the mean and standard deviation HU values of the selected ROIs that included the voxels in each density insert, and M_{center} and δ_{center} are the corresponding values for a centrally located ROI. The accuracy of the HU value in the ROIs selected in the density insert was then assessed by calculating the root-mean-square error (RMSE), which was defined as

$$RMSE = \sqrt{\frac{1}{N_{ROI}} \sum_{i}^{N_{ROI}} (M_{insert}^i - \overline{M_{insert}^i})^2}, \qquad (14)$$

where M_{insert}^i and $\overline{M_{insert}^i}$ denote the mean HU values of the ith ROI in the reconstructed and benchmark CBCT images, respectively, and N_{ROI} is the total number of selected ROIs.
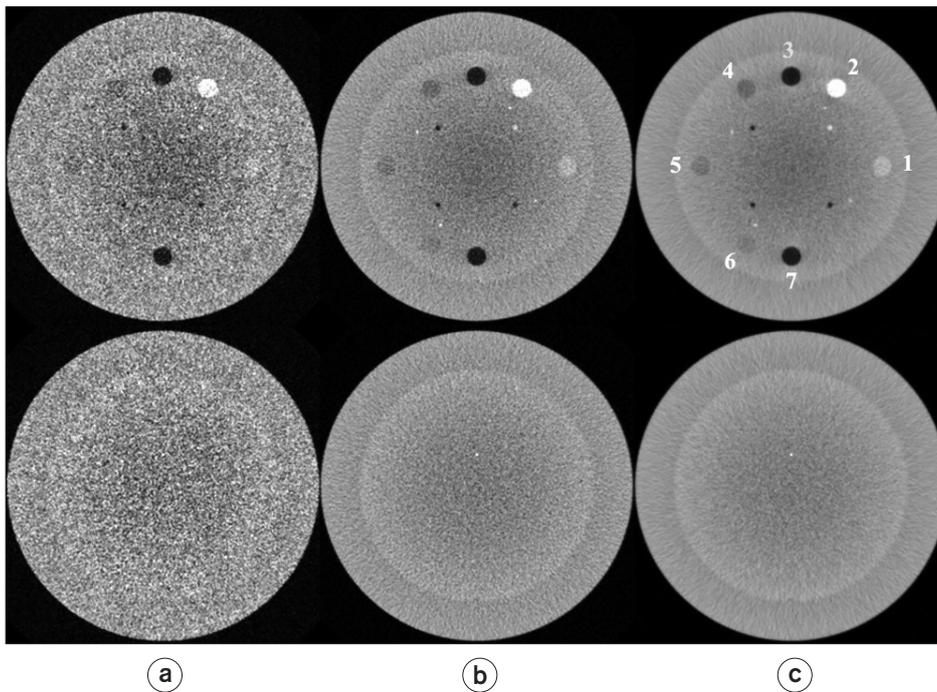
To further evaluate the overall reconstruction differences between the reconstructed and benchmark CBCT images, we calculated the correlation according to

$$Correlation = \frac{\sum_{i=1}^{N}(m_i^l - M^l)(m_i^h - M^h)}{\sqrt{\sum_{i=1}^{N}(m_i^l - M^l)^2 \sum_{i=1}^{N}(m_i^h - M^h)^2}}, \qquad (15)$$

where m_i^l and M^l are respectively the HU value at voxel i and the average HU values of the images reconstructed by the FDK with the Shepp–Logan filter, by FDK with a modified filter, and by the proposed methods using low-dose projection data. Equivalently, m_i^h and M^h are the HU values at voxel i and the average HU values of the benchmark image. N denotes all the numbers of voxels to be considered in the reconstructed images. In general, lower RMSE and higher correlation values yield better results.

Results

The performance of the ATV denoised FDK reconstruction algorithm was compared with those of the Shepp–Logan filtered FDK and the modified filtered FDK algorithms. Fig. 3 shows CBCT images of a representative slice of the phantom obtained by the three FDK algorithms. The
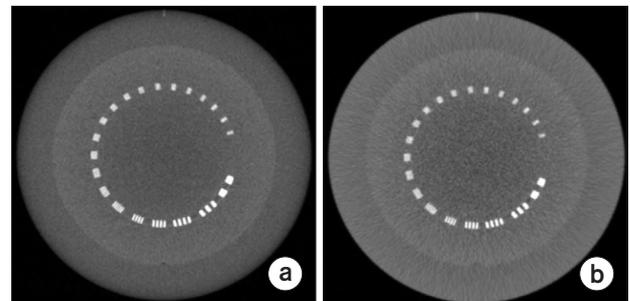
Fig. 3. Comparisons of the same views of the reconstructed image generated by applying (a) FDK with the Shepp–Logan filter, (b) FDK with a modified filter, and (c) FDK with ATV. The top row contains the CTP404 module and the bottom row contains the CTP486 module. All the images are displayed using W=1600 and L=200 HU.

Table 1. Comparison of contrast-to-noise rations at seven ROIs in the reconstructed images generated based on three FDK algorithms with low-dose projection data of the catphan503 phantom (CTP404).

ROI	FDK with Shepp-Logan filter	FDK with modified filter	FDK with ATV
1	3.15	6.29	11.69
2	5.50	12.94	23.66
3	4.84	11.59	23.14
4	0.05	0.48	1.36
5	0.38	0.81	1.64
6	0.87	1.58	2.76
7	5.14	11.64	23.09

Fig. 4. Comparison of reconstructed images for a representative slice generated by applying (a) conventional FDK using high-dose projections and (b) FDK with ATV using low-dose projections. These images, including the CTP528 module, are displayed using W=2400 and L=200 HU.

abrupt changes between adjacent voxels when the Shepp–Logan filter was used were significantly decreased by the application of the modified filter. After the addition of ATV denoising, the changes in the homogeneous region were more smoothed whereas features with different densities were preserved quite well. This indicates that the proposed method can spare noise effectively and avoids the heavy penalization of striking edges.

Furthermore, we calculated the CNR at selected ROI in the reconstructed image. It is possible to assess a comparison of relative image contrast between correspond-

ing regions. Table 1 compares CNRs at seven ROIs in the reconstructed image generated by FDK with the Shepp–Logan, FDK with the modified filter, and with the proposed methods. The proposed method shows the improved CNR in all the ROIs compared to the corresponding values elicited by the other two algorithms.

Fig. 4 shows the proposed FDK method with projections acquired at low mAs and the conventional FDK algorithm with projections acquired at high mAs to allow the qualitative evaluation of the correspondence between the two reconstructed images. It is observed that the proposed meth-

Table 2. Quantitative comparisons using two metrics in the reconstruction image generated by three FDK algorithms with low-dose projection data of catphan503 phantom (CTP404).

	FDK with Shepp-Logan filter	FDK with modified filter	FDK with ATV
RMSE	37.49	25.02	22.38
Correlation	0.943	0.966	0.971

od yields a spatial resolution comparable to high-dose CBCT imaging based on visual inspection. Table 2 lists two quantitative measures (RMSE and correlation) obtained from the reconstructed images based on the three FDK reconstruction methods. It is observed that the proposed method elicits a lower RMSE and a higher correlation compared to the other two algorithms.

Discussion

An improved FDK reconstruction algorithm for low-dose CBCT imaging has been developed by adding ATV denoising in the filtering process. The reconstructions of phantom data implemented with the proposed method indicate that a higher image quality can be achieved with projection data acquired with the low mA protocol. We have also found that the proposed method generated images with CNR values and spatial resolution comparable to the images reconstructed with projections acquired with the high-dose protocol. Moreover, ATV denoising elicited filtered projection data with a greatly reduced noise in comparison to conventional filtering. The alternative way for low-dose CBCT is to consider the use of compressed sensing (CS) in the iterative reconstruction algorithm.[13-15] The CS method is executed by minimizing a TV objective function subject to data fidelity and physical constraints based on constrained or nonconstrained optimization methods. However, in practical applications this approach is mainly limited by their high-computational demands because the reprojection and backprojection steps are iteratively performed for the fidelity calculation between measured and estimated projections.

Several edge preserving filters have been proposed for use to reduce the noise of fan-beam CT images based on the local characteristics of the projection data elements.[16] Unlike the fan-beam CT where the scatter signal is mini-

mized through the divergent collimator, the scatter signal of the CBCT projection data is not effectively suppressed through hardware only. The presence of the scatter signal can cause artifacts in the reconstructed CBCT image and can also alter the noise characteristics of the CBCT projection data.[15,17]

The ATV method works within the FDK framework, and provides increased speed owing to use of a single filtering and single backprojection processes. This analytical approach assumes that a sufficient number of projections are acquired during a single-gantry rotation. Thus, we identified the optimal parameters for ATV denoising by using the entire number of projections and by obtaining reconstructed CBCT images with higher quality given the noise suppression and edge preservation. The projections used in our experiments were acquired in small-FOV acquisition modes only. The method, however, has potential for applications in all imaging acquisition modes. In terms of computation time, the FDK with ATV denoising took approximately four times longer than the conventional FDK algorithm. Given that OpenMP was used to parallelize the proposed algorithm on the CPU platform, we can easily extend its use to the GPU.[18]

Conclusion

The proposed algorithm achieved imaging dose reductions in repeated CBCT scans with the use of low mA levels and also yielded high contrast-to-noise CBCT images. This was achieved by the removal of noisy corrupted areas, and by prevention of penalization of striking features. This work may have significant implications in image-guided or adaptive radiation therapy given the current, widespread use of CBCT.

Conflicts of Interest

The authors have nothing to disclose.

Availability of Data and Materials

All relevant data are within the paper and its Supporting Information files.

References

1. Nabavizadeh N, Elliott DA, Chen Y, et al. Image guided radiation therapy (IGRT) practice patterns and IGRT's impact on workflow and treatment planning: Results from a national survey of American Society for Radiation Oncology members. International Journal of Radiation Oncology* Biology* Physics. 2016;94(4): 850-57.

2. Lu L, Diaconu C, Djemil T, et al. Intra-and inter-fractional liver and lung tumor motions treated with SBRT under active breathing control. Journal of Applied Clinical Medical Physics. 2018;19(1): 39-45.

3. Yoganathan S, Maria Das K, Maria Midunvaleja K, et al. Evaluating the image quality of cone beam CT acquired during rotational delivery. The British Journal of Radiology. 2015;88(1054): 20150425.

4. Alaei P, Spezi E. Imaging dose from cone beam computed tomography in radiation therapy. Physica Medica. 2015;31(7): 647-58.

5. Wang J, Li T, Liang Z, Xing L. Dose reduction for kilovotage cone-beam computed tomography in radiation therapy. Physics in Medicine and Biology. 2008;53(11): 2897.

6. Feldkamp LA, Davis LC, Kress JW. Practical cone-beam algorithm. Journal of the Optical Society of America A. 1984;1(6): 612-19.

7. Ahmadi R, Farahani JK, Sotudeh F, Zhaleh A, Garshasbi S. Survey of image denoising techniques. Life Science Journal. 2013;10(1): 753-55.

8. Motwani MC, Gadiya MC, Motwani RC, Harris FC. Survey of image denoising techniques. Proceedings of GSPX 2004: 27-30.

9. Sidky EY, Pan X. Image reconstruction in circular cone-beam computed tomography by constrained, total-variation minimization. Physics in Medicine and Biology. 2008;53(17): 4777-807.

10. Perona P, Malik J. Scale-space and edge detection using anisotropic diffusion. IEEE Transactions on Pattern Analysis and Machine Intelligence. 1990;12(7): 629-39.

11. Wang J, Li T, Xing L. Iterative image reconstruction for CBCT using edge-preserving prior. Medical Physics. 2009;36(1): 252-60.

12. Sidky EY, Pan X, Reiser IS, Nishikawa RM, Moore RH, Kopans DB. Enhanced imaging of microcalcifications in digital breast tomosynthesis through improved image-reconstruction algorithms. Medical Physics. 2009;36: 4920-32.

13. Lee H, Xing L, Davidi R, Li R, Qian J, Lee R. Improved compressed sensing-based cone-beam CT reconstruction using adaptive prior image constraints. Physics in Medicine and Biology. 2012;57(8): 2287-307.

14. Sun T, Sun N, Wang J, Tan S. Iterative CBCT reconstruction using Hessian penalty. Physics in Medicine and Biology. 2015;60(5): 1965.

15. Lee H, Fahimian BP, Xing L. Binary moving-blocker-based scatter correction in cone-beam computed tomography with width-truncated projections: proof of concept. Physics in Medicine and Biology. 2017;62(6): 2176.

16. Wang J, Lu H, Li T, Liang Z. Sinogram noise reduction for low-dose CT by statistics-based nonlinear filters. Medical Imaging 2005: Image Processing: International Society for Optics and Photonics 2005: 2058-67.

17. Lee H, Xing L, Lee R, Fahimian BP. Scatter correction in cone-beam CT via a half beam blocker technique allowing simultaneous acquisition of scatter and image information. Medical Physics. 2012;39(5): 2386-95.

18. Park H-G, Shin Y-G, Lee H. A fully GPU-based ray-driven backprojector via a ray-culling scheme with voxel-level parallelization for cone-beam CT reconstruction. Technology in Cancer Research and Treatment. 2015;14(6): 709-20.